OPEN ACCESS
IOP Publishing
Journal of Physics D: Applied Physics
J. Phys. D: Appl. Phys. **54** (2021) 183002 (17pp)
https://doi.org/10.1088/1361-6463/abe07b

Topical Review

Ionic and molecular transport in aqueous solution through 2D and layered nanoporous membranes

M Caglar and U F Keyser

Cavendish Laboratory, University of Cambridge, J.J. Thomson Avenue, Cambridge CB3 0HE, United Kingdom

E-mail: m.caglar@me.com and ufk20@cam.ac.uk

Received 16 September 2020, revised 30 December 2020
Accepted for publication 27 January 2021
Published 16 February 2021

Abstract

Two-dimensional (2D) materials provide an intriguing means to not only study physical phenomena but also serve as disruptive membranes for ionic selectivity and sensing based applications. Atomic thinness of these materials affords a unique environment in an all-surface material to unlock challenges towards improving desalination, energy harvesting and DNA sensing. This review provides an overview on some common 2D materials used in membrane applications for solving these challenges along with opportunities where 2D materials could add value to existing solutions. Following this, different types of 2D materials and structures are discussed with their relative advantages and disadvantages highlighted. Fabrication and methods of creating pores within 2D membranes are then presented with a focus on altering surface characteristics. Selected works within the field are highlighted and placed into a wider context, comparing their merits and shortfalls. A discussion of state-of-the-art performance for ionic transport, molecular sensing and power generation is then presented. This review concludes with an outlook on emerging methods and discussing exciting future directions.

Keywords: nanopores, membranes, ionic transport, selectivity, DNA sensing, 2D

(Some figures may appear in colour only in the online journal)

1. Introduction

We are facing significant challenges to the ways in which we are currently living: the need to replace fossil fuels for cleaner alternatives is at a critical juncture; there are growing concerns over supply of drinking water; and there is an increasing scarcity of rare earth metals alongside a growing appetite for their consumption. One way to address these concerns is by the use of systems that employ a selectively separating membrane to extract material, salts or power from a concentration fed flow, as summarised in figure 1. For instance, ion-exchange membranes used within reverse osmosis (RO) systems [1] are able to desalinate and filter precious materials from waste water. Similarly, energy harvesting has been demonstrated using the selective ion flux from such systems [2–4]. However, currently these technologies are held back by challenges as described in figure 1(a), such as depending on externally driven processes which are energetically expensive, reducing the overall conversion efficiencies. There have been notable improvements in this regard, however opportunities

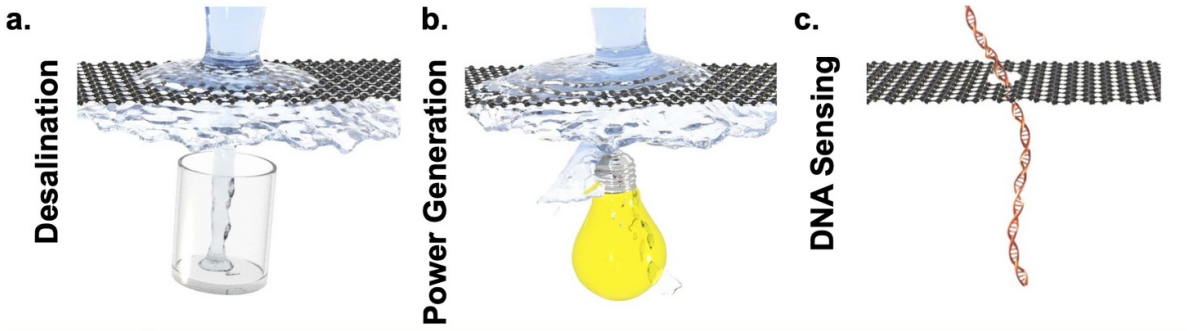

Process	Salt rejection	Osmotic energy harvesting	Resistive pulse sensing
Essential	Porosity control High flux High strength	High ionic selectivity Low current leakage Durability	Engineered pores Membrane/pore stability Low noise sampling
Goals	Complete water purification	Time stable, high power extraction per area	Base level DNA and single molecule detection
Challenges	Energy intenstive Membrane fragility Scalability	Surface/pore fouling Membrane fragility Thickness *vs.* power	Pore fouling / blockages Event SNR Event speed *vs.* sample rate

Figure 1. Desalination, power generation and DNA sensing applications are described in relation to two-dimensional (2D) materials serving as the ion-separating membrane. The physical process, essential attributes, goals and challenges are outlined for each application: (a) desalination, (b) power generation and (c) DNA sensing.

still exist for further process efficiencies in order to achieve commercial viability [4, 5]. A key improvement is employing systems which depend on salinity gradients to drive flow, removing the need for external pumping. Reverse electrodialysis and pressure retarded osmosis systems are examples of such systems but both require the use of low resistance membranes [6], for which thinner membranes are needed whilst maintaining mechanical stability, figure 1(b). As well as this, stacks of both cation and anion selective membranes [7], the latter of which has only recently been demonstrated [8].

The current ongoing global pandemic has also highlighted the importance of point-of-care (POC) diagnostics and the pivotal role they play within healthcare. Molecular sensing and characterisation is a critical part of POC diagnostics. Nanopores are able to discriminate between different analytes with adjustable specificity and are able to be miniaturised into mobile POC units such as the MinION (Oxford Nanopore Technologies) which uses a functionalised silicon nitride pore. The 1996 demonstration of sensing using biological alpha-haemolysin pores [9] coupled with an increasing aptitude of nanoscale systems reignited a fervent interest toward the field. Leading swiftly on from biological systems were solid-state platforms which would afford greater control over the design and behaviour of the sensing system. However, as in figure 1(c), increasing sensing resolution to detect yet smaller features coupled with accurate read-outs with high temporal resolution is an ongoing challenge [10] alongside reducing the fouling rate of both the membrane and pore used.

With these requirements and applications in mind, two-dimensional (2D) materials have, in the last decade, been demonstrated as attractive platforms for applications requiring control over both ionic and molecular transport. Although the discovery of graphene was the main instigator, the earlier arrival of nano-tubes and, later, 2D materials, has led to a broader focus on other low-dimensional materials, such as boron nitride and layered materials within the transition metal dichalcogenide (TMD) family such as molybdenum disulphide (MoS_2) and tungsten disulphide (WS_2). Within the 2D family of materials, control over key metrics such as the effective membrane thickness, surface chemistry and membrane porosity is critical in harnessing their potential. The wide range of adjustable parameters of 2D materials while leveraging their atomic thinness results in improvements which conventional materials cannot compete with. Moreover, functionalising or layering these materials still results in uniquely thin membranes whilst benefiting from diverse chemical and physical properties.

It has been demonstrated that 2D membranes can be tailored relatively easily toward these metrics which makes them promising candidates for use as ion exchange membranes [11]. Simply by virtue of their atomic thinness, many favourable transport properties are immediately afforded to these membranes as ionic/molecular separators or sensors. As materials approach atomic thickness an intrinsic flexibility alongside a decrease in fluid flux resistance occurs. By extension, the all-surface nature of 2D materials makes for a unique environment with which to study surface effects, alter surface chemistry and introduce defects/pores within the membrane. An example of an important consequence of this is the effect extrinsic surface charging has on the transport properties across the membranes [8, 12–14]. Therefore, 2D materials present themselves as an important platform both to

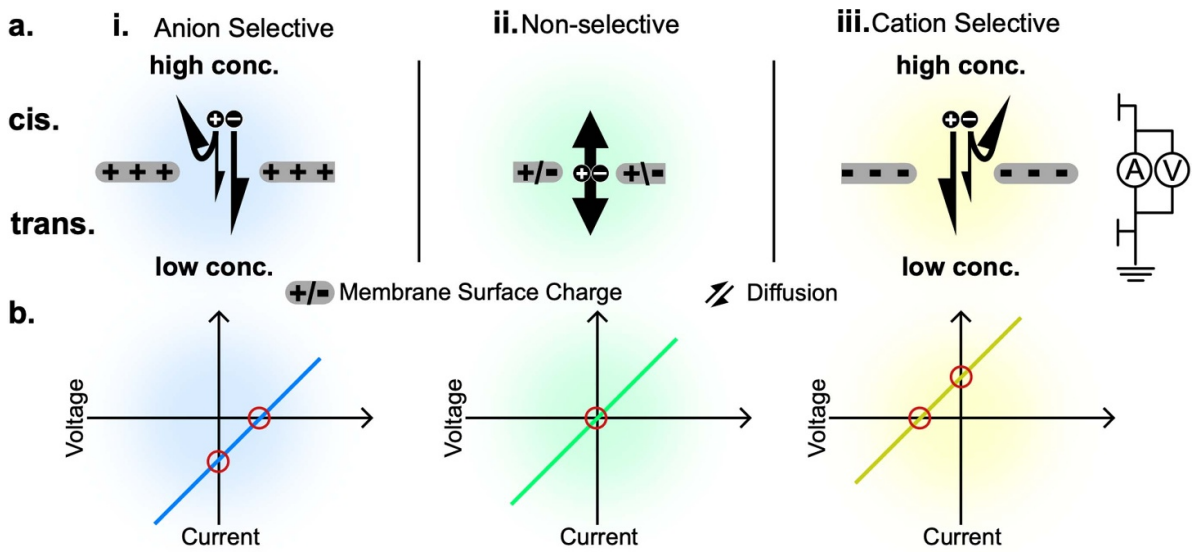

Figure 2. (a) A membrane possessing surface charge is separating a cis and trans reservoir, across which there exists a salt gradient. Electrodes, for instance silver/silver chloride (Ag/AgCl) electrodes, are within the reservoirs monitor the current and voltage (IV). Respective IV traces are presented in (b) for each case. (a)i A positively charged surface, and thus pore, exhibits anion selective behaviour with the IV trace showing a positive voltage offset and negative current offset (red circles), indicating anion dominated transport. (a)ii A neutral membrane, and indeed one with no concentration gradient, will not experience ion selective transport, with no current/voltage offsets. (a)iii A negatively charged membrane with cation selective behaviour and positive/negative voltage/current offsets respectively.

study transport phenomena but also in delivering exceptional performance.

In general, crystalline materials in their defect-free, pristine state are impermeable toward gases and ions (including protons) [15] (although there are some notable exceptions e.g. [16]). Thus for a 2D membrane to act as a porous selective separator it is necessary to create pores in the membrane. These can be introduced directly using a variety of methods such as, for example, electroporation [17] or chemical etching [18], or alternatively intrinsic ('native') defects occurring in transferred chemical vapour deposited (CVD) [19] materials can be utilised [8, 12]. The benefit of the latter CVD membranes is that they can be produced at volumes closer to commercial viability [20–22] whereas pores created by more specialised clean-room methods (e.g. ion beam drilling) can only be fabricated on a smaller scale. Furthermore, since 2D materials are synthesised bottom-up, they can be engineered with porosity or functionalisation tailored specifically for applications [23]. Moreover, larger scale treatments are being developed that can be applied to membranes to grow or shrink such intrinsic defects [12, 24–26].

In the following, the methods and techniques being employed to control the surface and ionic transport properties of 2D materials will be reviewed with a focus on their utility in emerging technologies. Firstly, an overview of different methods of synthesis and production of 2D membranes is provided within the context of selective transport facilitation—highlighting the lesser and more successful methods. Following this, appreciating the pivotal role that the surface and substrate play, different approaches toward controlling surface charge are assessed and how such control effects ionic transport and electrical properties with implications for sensing. Finally a brief discussion on the state-of-the-art performance for ionic transport, molecular sensing and applications thereof in desalination and power generation. Subsequently an outlook highlighting emerging methods and some exciting future directions concludes this review.

2. Mechanisms of transport

Passive transport across a porous membrane separating two reservoirs, cis and trans, figure 2(a), can be driven by a salinity gradient across the membrane. For an electrolyte, if the pore size is larger than one ion but smaller than another, due to steric selectivity, there will result an asymmetric ion flow. However such systems require precisely engineered pore sizes created in order to effectively discriminate between two ion diameters. For charged species, electrostatic effects will dictate the behaviour of this transport. Surface electrostatic charge effects are particularly important for 2D materials whereby surface and bulk effects are one and the same. For instance, on water, estimates for graphene surface charge are ~ -0.6 C m^{-2} [17] and ~ -0.16 C m^{-2} for hBN [27]. The exact mechanism creating this surface charge is currently not fully understood but is thought to be due to hydroxide adsorption around the edge of defects and nanopores [28]. For a non-selective membrane, anions and cations will jointly partake in the diffusion, resulting in no net charge across cis and trans reservoirs. If the transport across such a pore is asymmetric, the pore is said to be selective. The origin of such selectivity in most 2D material systems are primarily due to electrostatic based effects [8, 13, 14].

In figure 2(a) hypothetical cases for a charged semi-permeable membrane are presented. In all cases, the diffusion

led transport will result in net ion flow down a concentration gradient. For a positively charged, porous membrane separating a cis and trans reservoir as in figure 2(a)i, it is more likely for a greater population of anions to be at the pore interface. Therefore, the resultant diffusion will be more favourable toward transporting anions as opposed to cations. Therefore, a net movement of one type of ion would result in a measurable selective current and a subsequent reversal potential, V_{rev}, as described by the Nernst potential,

$$V_{\text{rev}} = S\frac{RT}{zF}\ln\left(\frac{C_{\text{trans}}}{C_{\text{cis}}}\right), \tag{1}$$

where $C_{\text{trans}}/C_{\text{cis}}$ are the concentrations in the trans/cis reservoirs respectively, R denotes the gas constant, T is temperature, z is ion valency, F is Faraday's constant and S is percentage of selectivity. As the name suggests, the reversal potential is the potential difference required in order to counter any charge flow. It can be seen from equation (1) that a system which is perfectly selective would have an absolute reversal potential of 59.5 mV per decade molar concentration ratio (M) (mV/log(M))—at 300 K. In such a system, there would be an exclusive transport of only one polarity of ion however, in real systems there tends to be some counter-ion flow reducing the selectivity. With an uncharged pore (figure 2(a)ii) which is larger than the ions that are participating in transport so as to exclude steric effects, no such asymmetric preference would be expected and thus no selectivity. Finally with a negatively charged surface (figure 2(a)iii) the increased population of cations close to the surface would likely result in a cation dominated flow.

Such ionic flow can be examined by applying a voltage and measuring the resultant current to obtain the current–voltage (IV) relationship for the system. The shape of these IV curves can be modelled by the Goldman Hodgkin Katz (GHK) equation [29]. Fitting to the individual IV curves allows the calculation of the relative permeability of the individual ions from which a selectivity can be extracted. However, a selectivity ratio can be obtained by fitting to the reversal potential which provides a ready comparison across a range of devices and systems. The form here is for a symmetric monovalent ion:

$$V_{\text{rev}} = \frac{RT}{F}\ln\left(\frac{P_{\frac{\text{cat}}{\text{an}}} + \frac{C_{\text{trans}}}{C_{\text{cis}}}}{P_{\frac{\text{cat}}{\text{an}}} - \frac{C_{\text{trans}}}{C_{\text{cis}}} + 1}\right), \tag{2}$$

where R, F are molar gas and Faraday constants respectively, T temperature, C concentration and $P_{\frac{\text{cat}}{\text{an}}}$ the selectivity ratio of cations relative to that of anions. In figure 2(b), an example of such an IV curve is presented for each case. Experimentally observed values can be fit to the expected GHK values in order to obtain the selectivity ratio ($P_{\frac{\text{cat}}{\text{an}}}$) as a fitting parameter. Despite the GHK model being devised in a time before 2D nanopores, the model shows good agreement with experimental studies in 2D systems [8, 17]. The applicability of the GHK model is limited by assumptions [30, 31], such as requiring constant electric field across the pore and membrane which has been confirmed by molecular dynamics studies within graphene [32]. Another is that permeant ions must not interact and are to exhibit concentrations at the membrane/pore proportional to those in bulk solution, the applicability of which is described well by Wen *et al* [33]. Finally, transport should be influenced by both concentration and electric fields. These assumptions hold for free solutions which are not close to saturation [31]. A caveat here would be that GHK could overestimate the osmotic potential if the surface conductance becomes significant compared to the bulk conductance. And indeed for small nanopores within monolayers, those that are of a high aspect ratio (pores are larger than the membrane is thick), a shift from bulk conductance has been reported [34]. In order to account for this an adjustment to the GHK equation could be made by weighting with the Dukhin number [24]. The Dukhin number includes this surface *versus* bulk conductance which is particularly important for pores up to ~10 nm [24]. Although this would make the model more robust, it would introduce assumptions about the surface charge of the membrane which are often difficult to ascertain. With this in mind, agreement between experimental data and GHK predictions [8, 17] would indicate that the physical processes underlying transport are well defined by electro-diffusion as described by the Poisson–Nernst–Planck (PNP) equations.

3. Pore geometry

Membrane thickness, pore distribution and pore size will dictate factors such as degree of selectivity, electrical and fluid resistance and sensing resolution. As almost all surfaces possess some surface charge, usually negative [35] as discussed, electrostatic effects are a significant contributor to these factors. When a negatively charged surface is exposed to an electrolyte solution, ions with an opposing charge will accumulate in order to screen this charge, referred to as a double layer. In the dilute solution regime [36], the Debye length, κ^{-1} , describes the distance over which the potential at the surface falls to $1/e$ of the value at the surface. This characteristic length is described by the following equation as well as the approximation for a monovalent symmetric electrolyte in water at 293 K,

$$\kappa^{-1} = \sqrt{\frac{\varepsilon_0\varepsilon_r R\,T}{2\cdot F\cdot\sum\frac{c\cdot z^2}{2}}} \tag{3}$$

$$\approx \frac{3.04}{\sqrt{I}} \qquad (z=1, T=293\ \text{K}), \tag{4}$$

where z is the ion valency, c is the ion concentration, ε_0 is the permittivity of free space, ε_r is relative permittivity, F is the Faraday constant, R is the gas constant, T is temperature and I refers to the total molar salt concentration. An oversimplified picture of ionic selectivity suggests that overlap in Debye lengths is required for a pore to be highly selective. In figure 3(a) the electric double layer is shown for a pore of diameter 15 nm in a 1 mM solution of KCl, a monovalent salt. The extension of the Debye length from the pore walls into

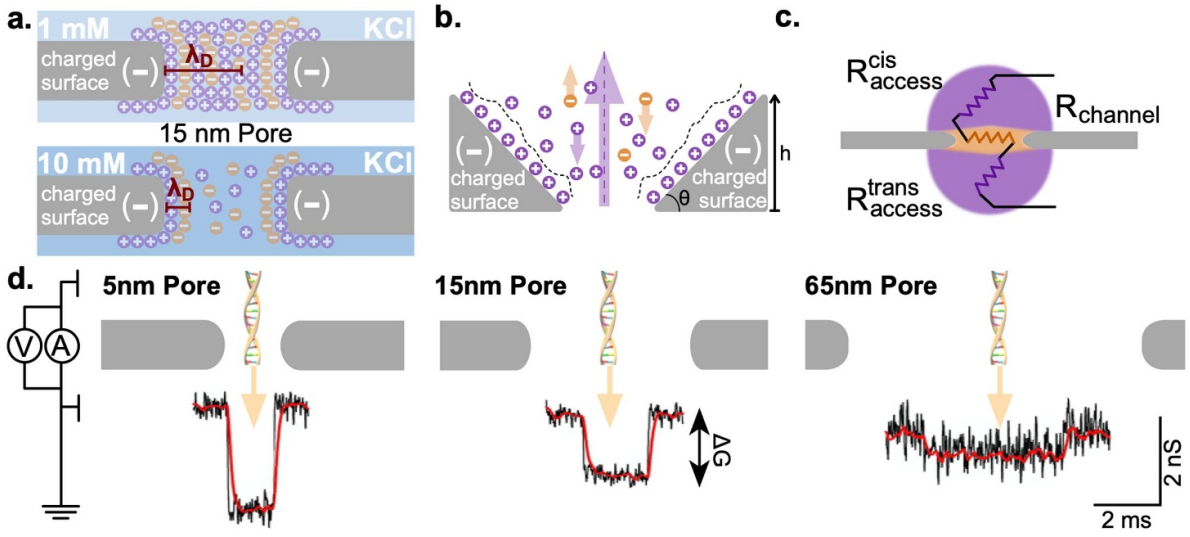

Figure 3. (a) Role of the Debye length in characterising pore channel charge. Double layer arrangement and Debye length shown for 1mM KCl, ∼10 nm and for 10 mM, ∼3 nm. (b) Ionic rectification effect demonstrated in a charge and geometrically asymmetric nanopore, with an internal potential difference causing an ion flow. (c) Pore conductance elements shown for a nanopore, highlighting contribution from access and pore resistances to the overall resistance. (d) DNA translocations through nanopores with differing pore diameters with representative current traces, indicating a tradeoff between event speed and sensing resolution. Panel (d) adapted with permission from [39]. Reproduced from [39]. © IOP Publishing Ltd. All rights reserved.

the centre indicates the areas under an effective electrostatic charge. For the same pore within a 10 mM solution, the limited reach of the electrostatic effects renders the centre of the pore electrically neutral, thus suppressing sensing and ionic selectivity. There are instances, however, when the Debye–Huckel linearisation approximation—for which equation (3) depends—does not adequately model the observed transport and sensing results. For example, for a concentrated electrolyte, equation (3) is no longer valid and a phenomena interpreted as increasing Debye length is reported with increasing ionic concentrations [37]. Similarly, highly charged surfaces move into a regime governed more by Dukhin length overlap due to increasing importance of surface (as opposed to bulk) effects [38].

Asymmetry in transport can also be a result of the shape and size of the pore leading to rectification of the current. Rectification, figure 3(b), where charge flows preferentially in one direction, is the result of several phenomena such as surface charge, selective transport and pore geometry [33]. Wen *et al* [33] attempt to disentangle some of these effects and find the pore angle and size to be significant contributors to the overall rectification ratio. Namely, the sidewall angle, θ as denoted in figure 3(b), should be less than 90° to observe rectification with no rectification for purely cylindrical pores ($\theta = 90°$). In addition, as θ approaches zero, the effective pore thickness, h_{eff} as in figure 3(b), will reduce. Rectification can be desirable and has been explored as a way to enhance selectivity and thus increase viability within energy harvesting applications [40].

The conductance of a pore is also an important consideration for pore characterisation. Figure 3(c) presents a pore within a thin membrane. Determining the conductance of a pore in such membranes are non-trivial as the membranes are relatively thin and thus access resistance effects are more significant. The pores therefore exhibit an access resistance [41] in addition to a channel resistance, taking these two parameters into account, and modelling the pores as having a hyperboloidal channel, as opposed to cylindrical, Kowalczyk *et al* [39] arrive at a pore conductance, G, formula of:

$$G = \sigma \left(\frac{4 \cdot l}{\pi \cdot d^2} + \frac{1}{d} \right)^{-1}, \tag{5}$$

where σ is the solution conductivity, l is the (effective) membrane thickness and d is the pore diameter. This relationship is supported by empirical evidence with a 20 nm silicon nitride (SiN) membrane. An interesting consequence of this model is that the membrane thickness could appear to be thinner than the physical thickness [39].

Monitoring conductance also underlines the use of nanopores as sensors by means of resistive pulse sensing techniques. As first demonstrated by Coulter [42], an absence of charge within the nanopore 'channel' due to the inclusion of a translocating species results in a conductance decrease, which manifests as a decrease in measurable current across the pore. Figure 3(d) demonstrates the expected conductance for a single translocation event across three pore geometries. As a consequence of both equation (5) and the relative electrostatic length scales (as discussed with figure 3(a)), larger pores result in a reduced sensitivity to a translocating molecule. The conductance response change therefore reduces in magnitude however increases in time, an important trade-off in signal-to-noise and sampling rate. Events that occur faster, with a greater drop in conductance, require a higher sampling rate and thus introduces amplifier limitations along with increased sampling of noise.

The pore size and membrane thickness will also impact upon the effective sensing region for a particular pore. The point at which the electric field drop is greatest is where the

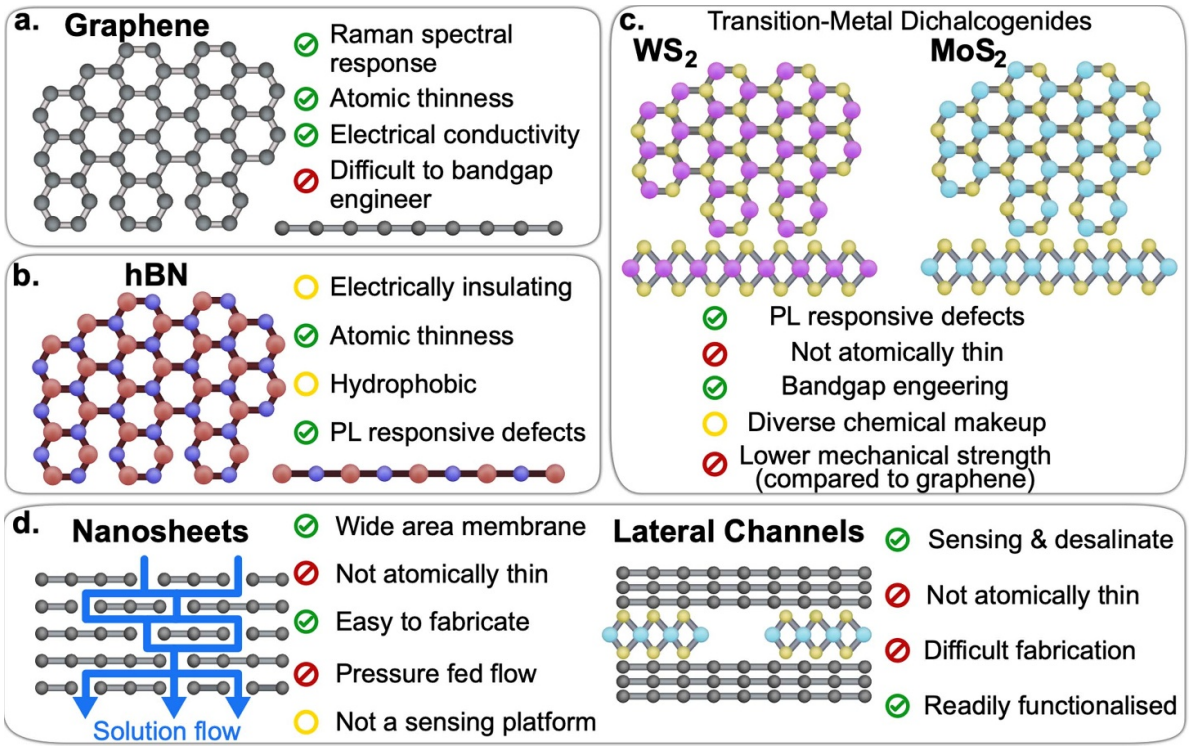

Figure 4. Selected advantages and disadvantages to some two-dimensional materials and structures as ion separating membranes are presented. (a) Monolayer graphene, (b) hexagonal boron nitride (hBN) and from the (c) TMD family, molybdenum disulphide (MoS_2) and tungsten disulphide (WS_2) is featured alongside (d) nanosheet membranes and those with 2D lateral channels.

sensing occurs and this coincides with the narrowest region. Therefore, in order to increase the sensing resolution, it is most desirable to make the sensing region as narrow as possible. Reducing the membrane thickness and pore diameter are two ways to accomplish this and translocating a well characterised molecule, such as DNA origami with features placed at known spacings [43], through such a pore would establish the sensing region [44]. However, both of these changes carry a reduction in total translocation time and thus require higher sampling rates which could be hindered by electronics with limited temporal bandwidth [45].

4. Types of 2D membranes

Within the group of 2D materials, graphene and hexagonal boron nitride (hBN) are two popularly grown membranes. Much work has focused on these two materials, with their diverse properties serving as good comparisons for performance. As a semi-metal, graphene is a very good electrical conductor with recent work demonstrating room temperature electron mobilities of $\sim$30 000 $cm^2\,V^{-1}\,s^{-1}$ for CVD grown graphene [46], figure 4(a). This is in stark contrast with, for instance, hBN which is an insulator, figure 4(b). Within the transition metal dichalcogenide family of materials, molybdenum disulphide (MoS_2) and tungsten disulphide (WS_2) have been used in promising applications such as solar cells [47], photodetectors [48] and single-layer transistors [49]. As a semiconductor with a band-gap controllable with the layering, MoS_2 presents another set of unique characteristics, which are summarised in figure 4(c). All four of these materials are widely grown using chemical vapour deposition (CVD) which is a scaleable process, enabling future fabrication of large area monolayer membranes. Alternatively these, and a whole host of other crystals, can be mechanically exfoliated, providing pristine 2D material but severely limited in area.

Moving away from atomic materials, there are a host of materials which are inherently thicker, such as graphene oxide, 2D materials supported on thicker materials or indeed stacked 2D materials. In figure 4(d), two such structures are highlighted—nanosheets and nano-lateral channels. These are formed from 2D materials into thicker structures which provide extra mechanical stability and leverage properties from other 2D materials in a heterostructure. Nanosheets membranes are particularly easy to fabricate and in relatively large areas however do not serve as sensing platforms and rely on an energetically expensive pressure fed system. On the other hand, lateral channels, though thicker overall, form a narrow angstrom scale channel which can be used for sensing and ionic selectivity. Their fabrication is trickier but the use of multiple materials results in ready functionalisability.

5. Substrate and surface treatment

Creating pores and altering surface properties of 2D materials remains an essential pre-processing step in subsequent use of 2D materials in most applications. These methods can range from intensive processes such as electron beam (e-beam) lithography to more *in situ* methods such as chemical etching. Here,

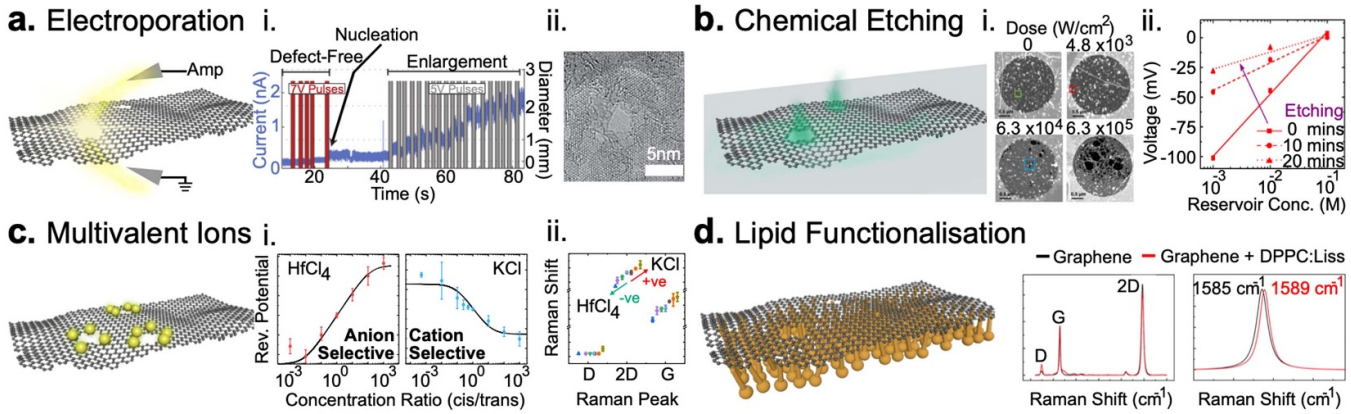

Figure 5. Surface treatment and fabrication of nanoporous membranes. (a) Electroporation used to nucleate defects and enlarging pores. Intrinsic defects in graphene are grown using chemical etching (b) as shown by changes in selectivity. Multivalent ions (c) and lipid monolayer (d) on graphene and hexagonal boron nitride (hBN) to alter surface charge as evidenced by selectivity and Raman spectra. Panels adapted with permission from: (a) [51, 52], (b) [12, 54], (c) [8], (d) [55]. Copyrights 2015 AIP Publishing; 2018 IOP Publishing; 2015, 2017, 2020 American Chemical Society; 2016 Royal Society of Chemistry.

an overview of these processes will be presented alongside a discussion of their merits and challenges.

5.1. Membranes with pores

Figure 5 presents methods which are applicable either *in situ* or, at least, outside of a clean room. Demonstrated by Kwok *et al* [50], applying voltage pulses across a silicon nitride membrane results in the creation of nanopores by causing a breakdown in the dielectric material. This was extended by Kuan *et al* [51] and applied to graphene, figure 5(a). The authors demonstrate the application of long 7 V pulses to a graphene membrane supported on silicon nitride (SiN) to nucleate a pore which they grow to a desired size by applying short 5 V pulses. This process was also shown to work for MoS_2 [52] with a TEM image of the subsequent pore shown in figure 5(a). This method of pore creation relies on using resistance measurements to characterise the size of the created pore. However, the simplicity of this electroporation method means it is difficult to ascertain as to whether or not a single pore is created, as opposed to a collection of smaller pores. Moreover, it is not possible to control precisely where pores are created. Therefore as a stochastic process, electroporation suffers from little to no control over the pore position and distribution [53].

As a similarly wide area treatment, two methods of chemical etching are shown in figure 5(b), (i) is a water assisted laser treatment of WS_2 [54] and (ii) is potassium permanganate ($KMnO_4$) *in situ* etching of graphene [12]. The WS_2 sample supported on SiN process achieved growth of existing defects and a minimum nanopore diameter of ∼15 nm. However, the photo-oxidation process for WS_2 was not demonstrated to have fine control at the smaller scale of pore diameters. In figure 5(b)ii the ionic selectivity toward KCl is shown for samples of graphene. The graphene is supported at the tip of a quartz nanocapillary and is immersed into a solution of $KMnO_4$ for up to 20 min. Walker *et al* [12] report a 4 times increase of membrane conductance at 20 min of etching and an almost complete reduction of ionic selectivity. Although not characterised by the authors, in order for selectivity to decrease to this level, nanopores would need to grow to a diameter of well over 100 nm [17]. Despite their merits, these methods suffer from a lack of control and the reliance on intrinsic defect structures for pore nucleation means that the success of these methods will heavily rely on, and vary with, the parts of a 2D material that are sampled.

Figures 5(c) and (d) present methods of altering surface charge of a 2D material. By a phenomena referred to as 'charge inversion', the charge on a surface can be flipped in polarity by use of multivalent ions [56–58]. This is demonstrated in figure 5(c)i with ionic selectivity trends across two salts for both monolayer graphene and hBN on quartz capillaries [8]. When measuring the transport of hafnium tetrachloride ($HfCl_4$), Hf^{4+} and Cl^- ions, Caglar *et al* find that the selectivity is dominated by anion transport [8]. In the monovalent case with potassium chloride (KCl) they find cation selective behaviour. Figure 5(c)ii further confirms this charge inversion by presenting the change in peak positions of the Raman spectra from graphene samples. For graphene floating on $HfCl_4$ the 2D and G peak positions are blue shifted indicating a more positive surface charge and the positions red shift for KCl, indicating a more negative surface. As a reversible process, this presents as an efficient *in situ* way to alter the surface charge, however is limited to certain salt conditions.

Figure 5(d) presents another way of altering the surface charge by exposing the surface of graphene to lipid groups [59] in a way which encourages formation of a unilamellar lipid layer on the surface of the material [55]. The charged nature of the lipid groups results in an effective surface charge shift as confirmed by shifts in the Raman spectral peaks. The authors also found that this temporary lipid layer provides the graphene with better mechanical and electrical stability. Their findings confirm previous work which demonstrated electronic modulation of graphene due to the presence of a lipid bilayer [60]. However, an increase in the effective membrane thickness due to the lipid groups is a less desirable consequence, alongside limiting the temperature and pH of

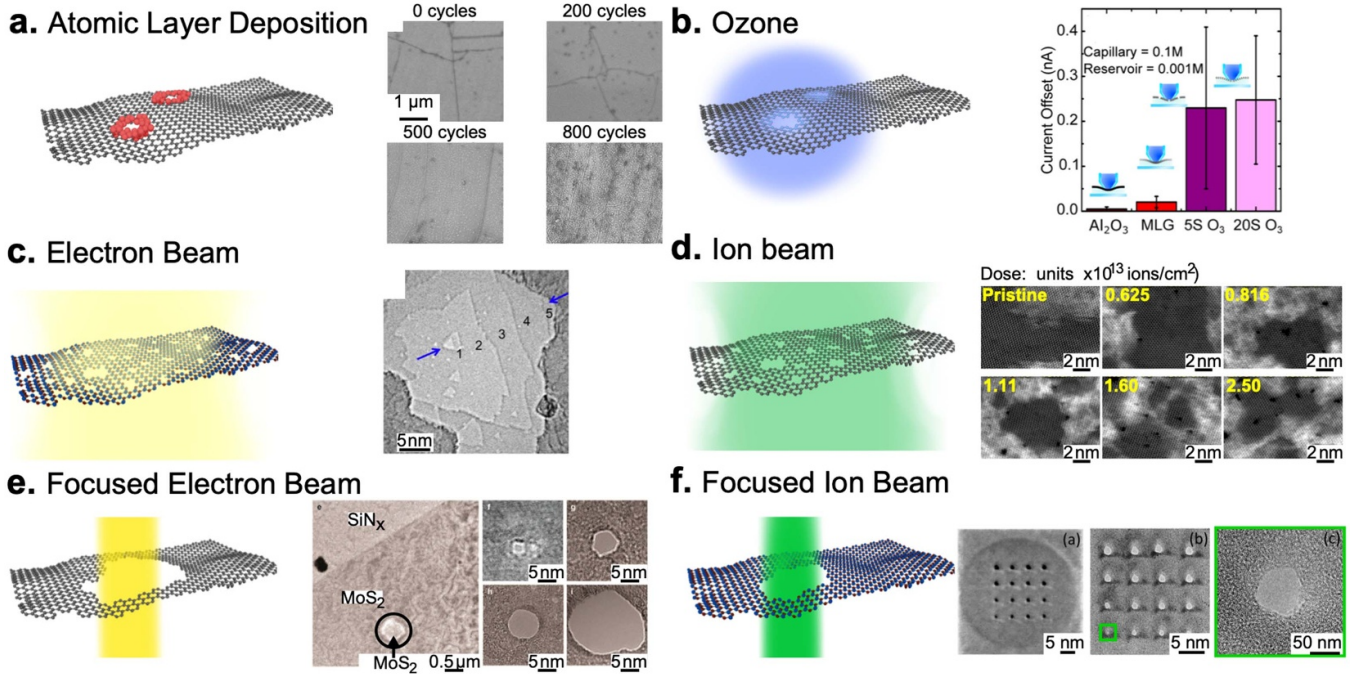

Figure 6. Surface treatment and fabrication of nanoporous membranes. (a) Atomic layer deposition of nickel onto graphene in order to reduce porosity. (b) Defects in graphene grown using ozone plasma treatment as shown by changes in selectivity. Focused electron beam (c) and focused ion beam (d) drilling alongside electron beam (e) and ion beam irradiation (f) to create and grow pores within graphene, hBN and molybdenum disulphide. Panels adapted with permission from: (a) [61], (b) [12], (c) [62], (d) [63], (e) [64], (f) [65]. Copyrights 2014, 2017, 2018, 2019 American Chemical Society; 2017 IOP Publishing; 2017 Springer Nature.

subsequent experiments in order to keep the lipid molecules stable.

In figure 6, clean-room dependant processes for altering porosity in 2D materials are presented. Although these are generally more intensive processes that come with higher experimental overheads, they allow a more controlled manner of both fabrication and characterisation. In figures 6(a) and (b) surface treatments that close and open pores respectively are presented. Figure 6(a) shows how atomic layer deposition (ALD) of nickel onto graphene can be used to fill defects [61]. The ALD layer is insufficient to evenly coat the membrane resulting in deposition preferentially coating defects before forming a thin film [12, 66]. In addition to nickel, alumina (Al_2O_3) deposition has been shown for graphene and it has been demonstrated that for a coated membrane, the selectivity level remain at levels similar to an untreated membrane [12]. However, the selective ion flux reduces [12] (figure 6(b)) indicating that the ALD is preferentially shrinking defects as opposed to coating the entire membrane. Exposure to an ozone plasma has been shown as an effective wide area treatment for both graphene [12, 18, 67] and hBN [68]. Walker *et al* [12] show that there are minimal relative changes to ionic selective transport across untreated graphene, graphene coated with alumina and also graphene treated with an ozone plasma. Although, perhaps expectedly [17] the voltage selectivity is similar across the treatments, the selective current, figure 6(b), is significantly altered. For a membrane undergoing a 20 s ozone treatment, the selective current is 8 times greater than the untreated CVD membrane, whilst through the alumina coated membrane a near-zero current is measured.

Electron and ion beam irradiation are powerful microscopy and fabrication tools. They can be used in a 'wide-field' irradiative manner or in a much more focused beam. Figures 6(c) and (d) present illustrative cases for electron and ion beam irradiation whilst figures 6(e) and (f) look specifically at focused beams. Exposing 2D materials, or thicker membranes such as SiN, to a high energy beam will cause some damage to the material surface. Continual exposure will cause nucleation of defects and subsequently opening of larger pores. These processes provide a high degree of control but are time intensive and thus suffer from low throughput. Moreover, unlike electroporation, they cannot create pores *in-situ* and instead must be carried out within a clean room by highly trained individuals.

Figure 6(c) demonstrates a use of electron beam irradiation as applied to hBN by Gilbert *et al* [62]. Upon exposure to an electron beam, the hBN layers are stripped in steps until a monolayer and then a nanopore remains, as indicated by the annotated '1' in figure 6(c). Crucially, the subsequent nanopore edge is atomically pristine. The authors note that when applying a similar method of pore fabrication to graphene, the subsequent pore geometry is highly irregular compared with the triangular pores seen for hBN [62, 69]. Another technique employed in pore creation using ion irradiation involves only nucleating defects [70] which can then be subsequently grown by other means, such as chemical etching or ozone treatments.

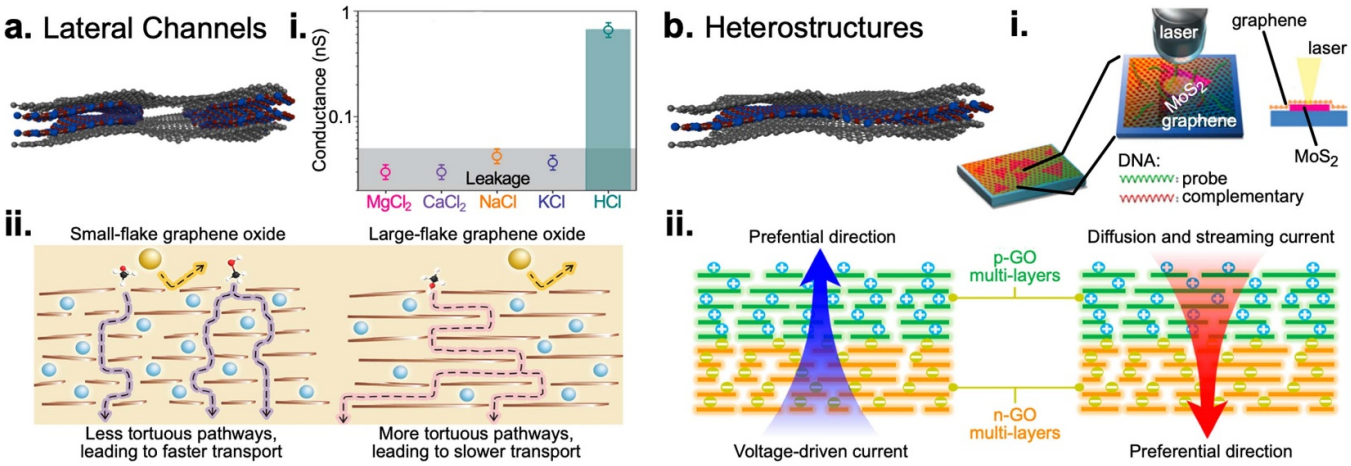

Figure 7. Layers of 2D materials to create a network of connected nano-channels. (a) Lateral channels formed using spacers, showing high ionic selectivity [85] and (a)ii formed using stacks of nano-flakes of graphene oxide (GO) [86]. (b) Membranes formed by layered materials, without spacers, to alter surface properties, (b)i MoS_2 and graphene structure used to sense DNA [87], (b)ii charged GO layers used to alter selective ion transport [88]. Panels adapted with permission from: (a)ii [86], (b)i,ii [87, 88]. Copyrights 2020 American Association for the Advancement of Science; 2019 American Chemical Society; 2014 John Wiley and Sons.

Beam exposure will cause damage to most materials, however, the nature of this damage could have consequences for the pore geometry and chemical make-up and will depend largely on the ion and its accelerating voltage [71, 72]. For instance, in MoS_2 the damage caused will result in preferential ejection of sulphur atoms from the crystal [73], and thus mono and di-sulfur vacancies are more predominant [74, 75]. In order to create pores in graphene, a higher displacement energy and thus beam current, when compared to MoS_2 or hBN [76, 77], is required and therefore it is more challenging to precisely create smaller pores [62]. Schneider *et al* [78] demonstrated pore creation using 300 keV in graphene, which is indeed too high for fine control. There are some conflicting opinions on the precise energy needed to eject atoms from graphene [76, 77, 79–81], however empirical observations have shown atom ejection to occur not only at lower energy levels of 60 keV [82] but also by use of an unfocused, relatively low energy beam to grow nanopores in graphene [70]. This is important as if these processes can occur at lower energies, there is greater control over pore size—especially at the smaller end. Furthermore, a lower beam energy would result in much less localised and long ranging damage being incurred.

Ion sputtering refers to the process of atom removal, or ejection, when accelerated ions are incident with a surface atom. An important step in sputtering is controlling exposure time in order to create a precisely sized pores. Li *et al* [83] found that sample temperature, ion beam duty cycle and the beam flux to be key parameters in determining the exposure time. Thiruraman *et al* also demonstrated the effectiveness of using photoluminescence (PL) as a characterisation marker when creating pores in MoS_2, they varied the ion dose until the PL from defects fell sharply [63]. Figure 6(d) presents an image of monolayer MoS_2 having been exposed to a variety of Ga^+ doses [63] producing defects by ion sputtering. Within ion irradiation, due to an ion being more massive than an electron the particle-surface interactions will be specific to the ion being accelerated. It has been suggested that ions cause greater displacement and atomic sputtering than that caused by electrons [71, 72].

Figure 6(e), f presents the case of focused electron and ion beams. Focused, or condensed, beams allow for precise single pore formation. Figure 6(e) shows the creation and growth of a nanopore in an exfoliated MoS_2 monolayer supported on silicon nitride [64]. A relevant advantage of using a focused beam for pore creation is that the pores tend to be stable over time and seem to, in graphene at least, not cause long range defects such as folding or warping which are typical artefacts from such methods of pore creation [84]. Moreover, this method affords flexibility in the sort of geometry produced that can be produced in addition to nanopores, e.g. nanogap or ribbon structures [84]. Finally, shown in figure 6(f) a focused ion beam produced a nanopore array in graphene [65]. Using a focused helium ion microscope (HIM), with exposure time controlled from 0.4 s up to 1.15 s in steps of 0.05 s, the array seen in figure 6(f) is produced. This demonstrates the control exercised over both the size and positioning of the pores.

Overall, wider area treatments such as those discussed in figures 6(a)–(d), enable a higher yield but at the expense of precise control whereas the lower yield processes (figures 6(e) and (f)) produce well characterised, high quality pores. All of these processes can be used in tandem with those discussed in figure 6, allowing the further growth of pores or altering the surface charge—leveraging the advantage of these more precise methods and those of the *in situ* methods.

5.2. *Layered membranes*

Moving from subtractive to additive processes, without dramatically increasing membrane thickness overall, 2D materials have been used as building blocks in order to form 2D channels. Figure 7(a) presents such a 'lateral' channel through a stack of 2D materials. A combination of monolayers of hBN/-graphene allowed Gopinadhan *et al* [85] to create channels of

only a few angstroms through which to study ionic transport. The results in figure 7(a)i demonstrate that mono and divalent ionic solutions are completely excluded through the channels whereas proton transport via hydrochloric acid (HCl) is permitted. Here, selectivity is dictated by the channel height in the lateral flow [89]. Mouterde *et al* [90] employ a similar device to study the streaming currents in long lateral channels in both graphene and hBN devices, showing the behaviour of ionic transport in confined channels. Channels with MoS_2 side walls have also been studied [91] and found similar confinement and steric exclusion.

In figure 7(a)ii a laminated graphene oxide structure is presented [86]. Flakes of 2D material, or graphene oxide (GO), are compacted into a membrane forming a network of connected nano-scale channels. Such laminated membranes are in themselves quite thick ($\sim$70 nm in this case) and are usually supported on yet thicker substrates. However, they are of note here due to high selective permeances achieved. Nie *et al* [86] used smaller GO flakes to form the laminated structure leading to faster selective transport through the membrane. Chen *et al* [92] use a reduced GO laminated membrane structure with angstrom scale channels providing orders of magnitude increased performance compared to conventional membranes. However, these membranes, though impressive, require significant driving pressure are not, overall, nanoscale. Finally, MXene membranes have been shown to facilitate selective transport via nanoscale channels [93]. Ding *et al* show that such membranes support both cation and anion selective behaviour and could extract up to $\sim$4.6 W m^{-2}, making important strides towards commercial viability.

Heterostructures, figure 7(b), made up of 2D materials could be devised to make use of characteristics from multiple materials in a single device. A graphene/MoS_2 heterostructure [87] presented in figure 7(b)i demonstrates how the bio-compatibility and aqueous stability of graphene is leveraged with the photoluminescent response of MoS_2 to create an electro-optical DNA sensing device. This demonstrates a novel way of measuring the presence and characteristics of DNA without the need of a nanopore. However, the heterostructure and lateral channels introduce added complexity within fabrication limiting larger scale applications. Although Loan *et al* report detection sensitivity for DNA in the attomolar range [87] detection across a material dimension greater than a single atom will always result in a lower theoretical sensitivity and resolution. Another approach has been the use of charged GO layers, figure 7(b)ii [88]. The authors stack negatively and positively charged GO multilayers forming a heterojunction leveraging the membrane polarities. Proton transport is seen to change its preferential direction depending on how the membrane flow is driven. This presents a tunable method of altering selective flow with potential for uses in energy and sensing applications. Such heterojunctions have been demonstrated using 2D materials; Lin *et al* [94] present a method of bottom-up growth of monolayer tungsten diselenide (WSe_2) on monolayer graphene. This flexibility in bottom-up growth highlights the advantage that 2D materials have in creating novel quasi-2D structures—albeit with significant fabrication overheads [94].

Thus, although these structures create an overall thicker membrane, the use of nano-scale channels preserve resolution performance. The fabrication is more difficult but enables functionalisation and combination of 2D materials within the structures, making use of diverse material properties.

6. Performance as salt separators

6.1. Ionic selectivity

Pores are necessary within membranes to facilitate both ionic and molecular transport. Therefore, demonstration of selective ionic transport and likewise by sensing translocating molecules, serve as common characterisation methods for porous membranes. However, beyond demonstrating membrane porosity, ionic transport is both important for understanding transport across membranes and for applications in desalination and power generation. Ionic selectivity, or ionic rejection, is accomplished by steric rejection/dehydration and/or by electrostatic repulsion [95]. For instance, charged functional groups at the edge of nanopores could be responsible for the electrostatic repulsion which lead to selective transport [96]. Related to this, chemical functionalisation at the edges of pores containing carbonyl groups are responsible for selectivity toward K+ versus Na+ ions [97]. This attempts to mimic the behaviour of biological pores.

Complementarily, steric and dehydration assisted salt rejection is shown clearly in controlled confined channels [85, 90, 91]. The confinement introduced by the nanopore or channel, is effective at steric rejection at, or just below the hydrated ion diameter—however, an entropic barrier is also introduced in pores at, or just larger than the hydrated ion. This barrier comes from the limited geometrical confirmations permissible for the ions passing through the pores, reducing the likelihood of passage [98]. Pore size is therefore an important factor in determining selectivity, figure 8 presents reported selectivity values as a percentage of *perfect* selectivity shown against the reported pore size. The colour of the data points refer to materials, whilst the symbols refer to the particular work.

Mogg *et al* use mechanically exfoliated hBN and graphene crystals on SiN apertures of 2 μm [16]. Using Raman spectroscopy, the samples are determined to be free of long range defects. Additionally, no gas permeation is measured through the monolayers, which would imply that the materials are defect free [15]. Having characterised the membranes, they proceed to measure selectivity with hydrochloric acid (HCl) and find that only protons are able to permeate through both graphene and hBN. Therefore, a selectivity of $\sim$100% is measured. However, no experimental results are shown with other monovalent salts or indeed any multivalent salts. This result would therefore remain as an outlier when compared to the remaining body of literature who insist on the presence of pores to accommodate transport across 2D crystals. As is evident from figure 8, a high degree of selectivity could be attained with only a $\sim$4 nm pore—characterising this magnitude of defect would be incredibly challenging with Raman spectra alone.

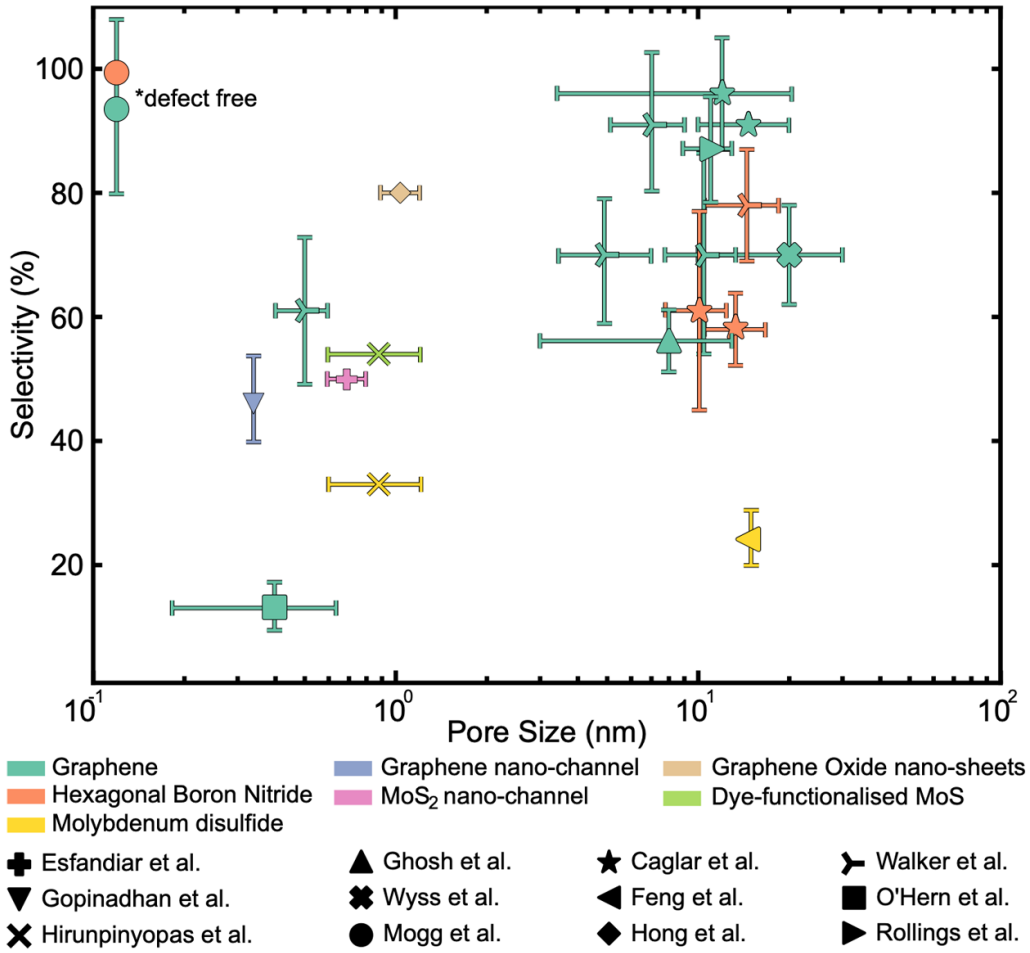

Figure 8. Reported values for ionic selectivity are presented against the reported pore size. Pore sizes are reported as circular diameters. Selectivity here refers to the percentage of the theoretical Nernst potential and is presented as an absolute percentage. Where pore sizes are not reported they are estimated from conductance data (Walker *et al*) and where selectivity is not explicitly stated, the reported membrane potentials are used. Data are from [8, 12, 16–18, 85, 91, 99–103].

Contrastingly, CVD membranes which have been wet transferred onto quartz capillaries are presented with a similarly high selectivity [8, 12]. CVD membranes exhibit defects which are intrinsic to both CVD growth and wet transfer processes [19]. However, the nature of relying on stochastic *intrinsic* defects results in a lack of control and high variability across samples. When characterised, Caglar *et al* found a combined total pore size to vary across both hBN and graphene samples ranging from 10–20 nm [8]. The authors sealed monolayers onto quartz capillaries with a ∼150 nm opening to measure the ionic transport for a variety of salts, shown in figure 8 is for KCl and $HfCl_4$ [8]. In graphene, a total combined pore size of 21.8 ± 9.2 nm was found to have a cation selectivity of 91%, meanwhile the hBN sample has a total defect size of 13.3 ± 3.18 nm and selectivity of $58 \pm 6\%$. Using multivalent ions the authors find that due to surface charge inversion, anion selectivity is reported—graphene with defects of 12 ± 6.6 nm achieved anion selectivity of $96 \pm 9\%$ and for hBN 10.1 ± 2.3 nm, $61 \pm 16\%$ anion selectivity.

Walker *et al* [12] use a similar method and therefore, here also, the reported conductances are used to estimate pore sizes and thus represent the summed total defect area. The hBN samples had a combined defect area of equivalent to a circular pore of diameter 14.5 ± 4 nm with a $78 \pm 9\%$ selectivity. Across the graphene samples, the pore size was on average 7 ± 3.6 nm with a cation selectivity of $92 \pm 13\%$. ALD surface treatments applied to closing pores reduced the size to 0.5 ± 0.1 nm and selectivity reduced to $61 \pm 12\%$. Meanwhile, ozone plasma was used to grow pores to 5.4 ± 1.9 nm and 10.5 ± 3.3 nm with almost identical cation selectivities of $\sim 70 \pm 15\%$ but with reportedly higher selective fluxes [12]. This indicates that both ALD and ozone treatments are effective in controlling selective flux, and thus extractable power, whilst maintaining selectivity.

As discussed previously, electroporation suffers from a similar reliance on overall membrane conductance to infer the total pore size but provides a method of altering porosity with a reasonable degree of control. Rollings *et al* use electroporation on CVD grown graphene samples supported on a SiN substrate [17]. Pores of varying sizes are created and grown using this technique. The cation selectivity with KCl ranges from $81\% \pm 13\%$ to $92\% \pm 5\%$ for $7 \pm$ nm 2 and 11 ± 2 nm respectively. Rollings *et al* also report observing selectivity up to a pore size of 100 nm, consistent with many others [8, 101, 104].

Electroporation has also been demonstrated with monolayer MoS_2 on SiN [101] both TEM and electroporation are used to create pores. Selectivity is reported for a 15 nm pore with $23 \pm 3\%$ cation selectivity for KCl.

Ion beam created pores in polymer (PET/PCTE) supported CVD graphene are used to measure ionic selectivity [18, 102]. In the case of O'Hern *et al*, the graphene is first exposed to an ion beam to introduce defect sites which are then grown by an etching process. Pore sizes are estimated at 0.4 ± 0.24 nm. Membrane potentials are estimated from a measured cell potential using activity coefficients. This yields a peak 4 mV offset for a 10 minute etch. The value is obtained with KCl at 0.5/0.167 M concentrations corresponding to a $12\% \pm 4\%$ selectivity. This is surprisingly low and within the bounds of experimental error [18]. Similarly, Ghosh *et al* use heavy ion beam irradiation to create pores on the order of 8 nm with a reported selectivity of $\sim 54 \pm 6\%$ towards monovalent salts [102], which is lower than expected levels. For instance, Wyss *et al* also used a polymer film support (PCTE) [103] with the a double layer of graphene used in order to provide extra structural stability. Etching is carried out through a mask to achieve pores of around 20 ± 10 nm. Selectivity toward cations in LiCl is measured to be around $70 \pm 8\%$, which is more in line with expected values for monovalent cation selectivity.

Also worth mentioning here are nanostructures created from nanomaterials that are not in a monolayer form. As discussed earlier, Gopinadhan *et al* measure complete salt rejection through channels as small as 0.3 nm [85]. Specifically, they measure no conductance for mono- and di-valent salts, with the exception of HCl for which they observe conductance. This implies a salt rejection of 100% across salts. Selectivity is estimated from the provided data—voltage offsets are reported as 24 and 32.3 mV which are used to calculate a selectivity of $47 \pm 7\%$. Similarly, Esfandiar *et al* use thick graphitic layers that are sandwiched with a monolayer MoS_2 spacer forming a long nano-channel measuring around $0.7\ \text{nm} \pm 0.1$ nm achieving a selectivity of around 50% toward cations in KCl [91]. These studies highlight that high levels of selectivity can be attained in thicker, and thus stronger, membranes.

Finally, so called 'sieving' of ions are achieved by stacking cascading nanosheets creating irregular paths through the structure. Hirunpinyopas *et al* demonstrate the use of stacked nano-sheets of MoS_2 atop a polymer supporting film (PVDF) to form a membrane. The formed nano-channel is estimated at $0.9\ \text{nm} \pm 0.3$ nm. Selectivity is measured toward $AlCl_3$ which means the cation possesses a $+3$ charge—thus requiring some caution when comparing to monovalent ions. A cation selectivity of 33% is reported. Upon functionalising the walls of the nano-channel, the selectivity is increased to 54% [99]. A similar finding is reported by Hong *et al* using nanosheets of graphene oxide providing 1.05 ± 0.15 nm channels supported on Si with a cation selectivity with KCl of $\sim 80\%$ [100].

Overall, figure 8 demonstrates that a range of selectivity levels across materials have been shown in literature. Studies featuring very small pore sizes, around 1 nm, report selectivity levels less than 60% whereas a bulk of work report values closer to *perfect* selectivity for pore sizes of around 10 nm and above. Recently, Thiruraman *et al* [105] created sub-nanometer pores in MoS_2 finding them to be almost non-selective as the pore sizes are comparable to the hydrated ion size. Membranes consisting of such very small pores results in a very high resistance and thus introduces difficulty in measuring much smaller currents. Therefore, these structures are not only easier to fabricate but also reduce the membrane resistance/increase the selective flux.

6.2. Desalination and energy harvesting

The clear application of this selective transport is in desalination. However, with most membrane based systems reliant on pressure to force fluid through the membrane, the systems became less energetically favourable, as discussed in figure 4. Graphene oxide and other 'sieving' membranes are popular candidates. For example, Hirunpinyopas *et al* [106] presents the feasibility of dye-functionalised MoS_2 laminar desalination using pressure, achieving higher salt rejection compared to GO. Without using pressure, Surwade *et al* [67] demonstrates desalination through perforated monolayer graphene supported on silicon nitride. Pores are estimated at $\sim$1–2 nm created using oxygen plasma exposure and thus distributed over the whole membrane. Raman spectral peak intensities characterised the membrane with the d-peak and g-peak ratios as $I_D/I_G = 0.6$ indicative of significant defects. They achieved a 99% reduction in permeate conductivity and filtered 2.6 ml over a 24 h period. This compares to only a 29% reduction in permeate conductivity and 7.5 ml filtered from a SiN pore. This indicates clearly that graphene has a significant to role to play compared to more traditional membranes such as SiN. However, the relatively low yield of filtered water presents the challenge—applying pressure would reduce energy efficiency and could rupture the thin membrane but could increase the yield.

Closely related to demonstrating ionic selectivity is the ability to extract power from such a membrane. Commercially applied pressure retarded osmosis membranes achieve around 1–10 W m^{-2} with the likes of Nafion and polymer membranes falling in this range also [107]. For single pores in MoS_2 ranging from 2 to 20 nm, Feng *et al* report 1 nW power extraction per pore with a density of 3×10^6 W m^{-2} [101]. For pores in graphene, the estimations are less than that of MoS_2 but greater than a commercial nafion membrane. Both Walker *et al* and Rollings *et al* calculate an extractable power of $\sim$700 W m^{-2} through graphene pores [12, 17]. Whilst Caglar *et al* estimate this to be in the range of $1\text{–}2 \times 10^4$ W m^{-2} for both graphene and hBN exhibiting an average combined pore size of $\sim$20 nm. Overall, the competitive promise of these membranes in power extraction demonstrates how disruptive 2D materials can be if the challenges presented in figure 4 can be overcome, primarily, membrane fouling and enclosure design such that high pressures can be withstood [108, 109].

7. Performance as DNA sensors

Demonstration of DNA and molecule transport across nanopores enables the nanopore system to be used as a sensor and also confirms the presence of nanopores of at least $\sim$3 nm

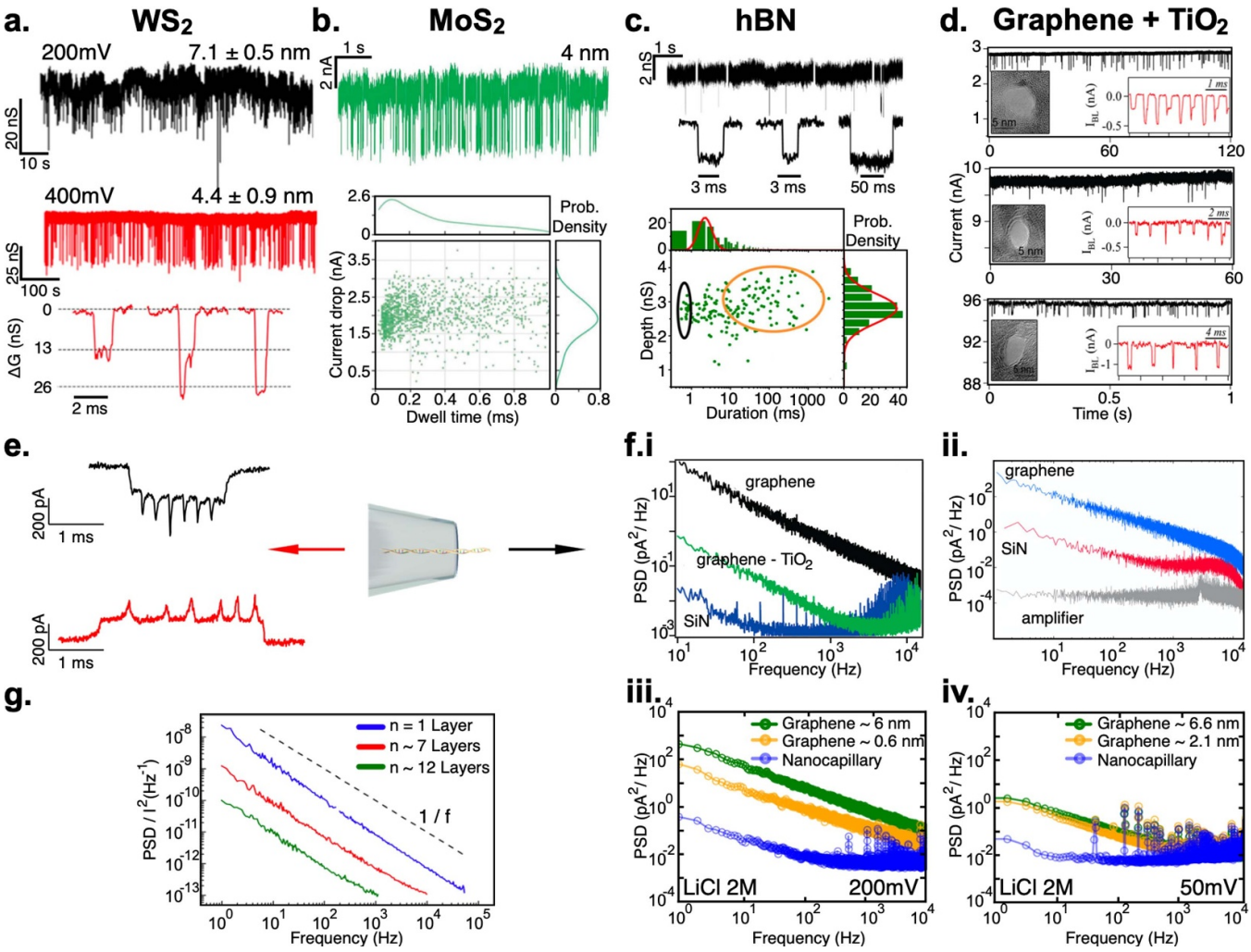

Figure 9. (a) Tungsten disulphide membrane with ∼7 and ∼4 nm pores shown to sense translocating double stranded DNA (dsDNA) molecules with a close up of select events [111]. (b) dsDNA translocation events shown through a 4 nm pore in molybdenum disulphide alongside a scatter plot indicating some event discrimination [116]. (c) Translocations of dsDNA through a 4 nm pore in hexagonal boron nitride (hBN) [113]. (d) Translocations through titanium dioxide (TiO_2) supported nanopores in graphene [112]. (e) Single translocation events shown in the forward, black, and reverse, red, directions of dsDNA hairpin structures through a glass nanopore [43]. (f)i, (f)ii: Noise characteristics are compared for suspended graphene [121] and TiO_2 supported [112] along comparisons to silicon nitride (SiN) membranes. (f)iii, (f)iv: present noise characteristics for electroporation created pores in graphene suspended on glass compared to the noise in 'as-grown' graphene and the glass alone. (g) Noise characterises are shown for a range of layers of graphene, highlighting reduced 1/*f* noise as the layers increase [122]. Copyrights 2010, 2017 American Chemical Society, 2020 John Wiley and Sons, 2013, 2017 Springer Nature, 2015 IOP Publishing and 2013 AIP Publishing.

diameter in the membrane. Surfaces and nanopores within 2D materials hold great promise in the sensing area, with recent work suggesting that small defects in DNA backbones could even be detected [110]. The chief tradeoff in nanopore sensing systems are to do with the sensing resolution and the signal-to-noise ratio (SNR). Atomically thin membranes achieve a very high sensing resolution but introduce a tremendous amount of electrical noise, making the signal harder to interpret. Also, a thin membrane results in a fast translocation time, requiring high sample rate amplifiers which add complexity and additional noise. In figure 9, some demonstrated translocations across a range of materials are highlighted, alongside discussions around performance and tradeoffs. Further, challenges such as noise and molecule discrimination are discussed with examples.

Tungsten disulphide (WS_2) monolayers exhibit a direct band gap and strong photoluminescence (PL) in the visible range, opening possibilities for advanced optoelectronic applications [111]. Danda *et al* use focused electron beam to create pores of about ∼4–6 nm in diameter on silicon supported WS_2. Translocating 15 kbp double stranded DNA (dsDNA) through the pores results in the traces seen in figure 9(a). For the 7.1 nm pore shown in black, the accelerating voltage is 200 mV, resulting in a slower translocation time but a much noisier baseline current when compared to the 400 mV used for the red trace. In both cases, they find that translocations occur in three orientations, as shown by the three traces, unfolded, partially folded and folded. Unfolded translocations account for 22% of events for the larger 7 nm pore and only 4% for the smaller 4 nm pore—these are in

line with other observations [64, 112, 113]. The authors use a high concentration (3 M) of KCl for the translocation experiments due to the reported reduction in DNA-graphene interaction [114]. Reduced interaction would reduce the likelihood of pore blockages however could also decrease the translocation time or discourage pore entry altogether [115] due to a reduced population of DNA around the pore.

Recently, Thakur *et al* demonstrated wafer scale fabrication of devices capable of nanopore sensing [116]. The authors use monolayer CVD MoS_2, through which DNA translocations have been demonstrated previously [64]. The authors demonstrate that short strands of 100 bp dsDNA can be sensed through a 4 nm pore created using electroporation. Sensing much shorter strands of DNA are more challenging given the faster translocation times. Figure 9(b) shows the current trace obtained from the events with a 500 mV driving voltage. Overall, the authors observe a current drop of ∼25% which is in line with other observations seen with dsDNA through MoS_2 [73]. The authors find that dwell times for the translocation events are increased [117] relative to studies with other materials. This is due to DNA interaction with 2D surfaces, including MoS_2, with such interaction increasing likelihood of populations of DNA in the affinity of the pore. A consequence of this is the observed increase to translocation times. Another is an increase in pore blockages. Moreover, molecular dynamics simulations have also shown that pore engineering techniques could slow down translocations across MoS_2 pores [118]. It has also been shown that the surface of MoS_2 can be used to detect DNA presence with very high mass sensitivity (∼3zg) [119] and attomolar concentrations [120], although detailed information of the DNA structure is less easily inferred from these methods.

In figure 9(c), an example of translocations through a 4 nm TEM drilled pore on hBN is shown [113]. Exercising control over this TEM drilling will dictate the geometrical makeup of the pore which is known to alter base level resolution [123] in hBN. A mixture of 48.5 and 10 kbp dsDNA in 1 M KCl is used with an accelerating voltage of 150 mV. The authors are able to detect these translocation events which show some discrimination in the peak depth versus duration scatter plot. Notably, Zhou *et al* find that a UV-Ozone treatment can be used to decrease the hydrophobicity of hBN—reducing the contact angle from 57° to 26°, significantly increasing pore wetting [113]. The hydrophobic nature also results in reduced dsDNA interactions the hBN surface, compared to graphene, indicating that translocations could occur in a stall-free manner [10].

Merchant *et al* demonstrate DNA translocations through graphene nanopores [112]. Pores are created using TEM drilling with translocations demonstrated for 22 nm pores. However, the authors found the noise of such large suspended areas of graphene to be overwhelming, diminishing the SNR. In an effort to reduce the noise, Merchant *et al* coat the graphene with 5 nm of titanium dioxide (TiO_2) which was found to reduce the noise by several magnitudes [112]. Figure 9(d) represents the translocation events from the subsequent coated membrane—with pore sizes of ∼7 nm. The top two traces are from similarly sized pores with 100 mV driving voltage and 1 nM of 15 kbp dsDNA. Despite identical setups, the conductance, baseline noise and events do not coincide. This suggests that the pore geometry, graphene quality and TiO_2 coating homogeneity will have significant effect on the DNA–graphene interaction. The final trace is for a similarly sized pore with 20 nM of 400 bp dsDNA being driven by 150 mV—once again the pore conductance scaling is inconsistent. This highlights a difficulty in altering a monolayer with a surface coating with a sufficiently thin layer as to not compromise the unique qualities of the 2D monolayer. Similarly, Rodríguez *et al* have decorated graphene nanoribbons with iron oxide nanoparticles (Fe_3O_4), demonstrating single and double stranded DNA sensing with noise an order of magnitude lower than un-decorated graphene [124]. Finally, with an alternative take on the matter, Ganguli *et al* functionalise DNA strands instead of the surface [125]. The graphene field effect transition (GFET) device leverages graphene's high DNA absorption in order to increase sensing sensitivity [125].

In an effort toward achieving DNA sequencing through 2D nanopores, an iterative step could be sensing molecules attached to a DNA molecule. An example of such a structure is a so called 'DNA ruler' which is a 7228 bp dsDNA strand with DNA folds every 1032 bp containing a total of six folds [43]. The expectation would be that the translocation of such a molecule would result in six measurable peaks in the conductance changes. Figure 9(e) presents data of such translocating events through a 14 nm quartz nanocapillary by Bell *et al* using 4 M LiCl and a 600 mV driving voltage. The authors find that the resultant translocation events present the expected peaks and can be seen in both forward and backward directions as depicted. Achieving performance comparable to these solid state pores but through 2D nanopores is an outstanding challenge and perhaps will be a defining one for the future use of 2D nanopores in a sensing application.

This demonstrates clearly the common problem with 2D nanopores and membranes in general; a high degree of noise with SNR levels which make event detection very difficult. One way around this is to support membranes which will sacrifice the overall thickness but, as found by Zhou *et al* [113], results in a significant reduction of $1/f$ noise in hBN pores when the supporting window is increased in size. Similarly, Merchant *et al* find that noise through graphene nanopores are several orders of magnitude higher than SiN nanopores—the noise fluctuations are reduced only with a 5 nm ALD of titanium dioxide [112] as shown in figure 9(f)i. Similarly, in figure 9(f)ii. [121], noise characteristics through graphene with a 10 nm pore is compared against SiN. Once again, graphene exhibits significant low frequency noise which is two orders of magnitude higher than the SiN membrane when considering the $1/f$ dominated noise. In both figures 9(f)i and ii the bias voltage is 100 mV.

In figures 9(f)iii and iv the noise is shown for a graphene membrane suspended on a quartz nanocapillarly as described previously [8, 12]. In both figures 9(f)iii and iv, the nanocapillaries have a ∼150 nm opening and are filled with 2 M LiCl. The three traces, blue, yellow and green, are obtained for the same set of capillary/graphene. In 9(f)iii the applied voltage is 200 mV, considering the lower bias voltage, the capillary platform compared favourably with the SiN shown in figure 9(f)ii

[121]. The yellow trace shows the noise characteristic for the nanocapillary with CVD graphene suspended across the opening. In figure 9(f)iii, this sample has a collective defect area equivalent to a circular pore of diameter 0.6nm whilst figure 9(f)iv has 2.1 nm.

In both cases, the noise is comparable to the suspended graphene in both figures 9(f)i and ii indicating similar characteristics across these samples. Within figures 9(f)iii and iv, the green traces show the noise for the CVD membrane (yellow trace) after a pore is created via electroporation. The noise of the graphene membrane with a ∼6 nm pore is an order of magnitude higher than without the pore. This is consistent with other observations that by decreasing the amount of 2D material which is supported—thus increasing suspended regions—increases the overall noise of the membrane [112, 113, 121]. This notion is further cemented in figure 9(g) which presents the noise spectra for layers of graphene membranes. Shown here, is that the overall noise magnitude decreases significantly with additional layers of graphene [122].

Overall, DNA translocation across suspended monolayers have been demonstrated however significant shortcomings are identified. Several trade-offs are at play: membrane thickness increases stability but reduces resolution; larger suspended regions increase noise but also resolution; faster translocations result in a more dramatic conductance peak however require higher sampling to capture. Enhancements and tuning across these various trade offs, by altering membrane thicknesses, supporting structures and salt conditions will result in optimal parameters to be found that balance these trade-offs.

8. Outlook and conclusion

Two-dimensional materials are still emerging and despite their infancy, have shown significant promise for improving future performance in power extraction and molecular sensing. However, remaining challenges are preventing their commercial success. Despite recent work on roll-to-roll CVD manufacture of graphene [22, 126, 127], upscaling membrane fabrication to commercial levels is still a challenge. Moreover, there still remains gaps in understanding the precise effect of membrane porosity both on selectivity and power extraction. For instance, it is thought that for atomic membranes, conductance scales in a less than linear fashion with membrane porosity [128]. And indeed, recent simulations have shown extractable osmotic power to, initially, increase with porosity but at a certain point show a sharp decrease [129]. Furthermore, in addition to pore distribution, pore geometry plays a pivotal role in rectification which in turn affects both leakage currents and extractable power as well as ionic selectivity [130]. Fundamentally, however, shortcomings discussed previously pertaining to the monatomic thickness of membranes must be overcome—namely relating to SNR and mechanical stability. These are particularly pertinent when considering mechanical strength, pore fouling and sensing resolution. Overcoming these trade-offs will result in sacrificing either sensing/selectivity performance or mechanical strength. The future for these membranes is certainly hopeful, with so many improvements demonstrated both in understanding physical phenomena and nano-fabrication in the last decade. As this review mainly addressed application in aqueous solution, it is worth noting that there is significant research in the area of gas separation and sensing with 2D membranes [131–133]. Most recently, impressive selectivity ratios of 32 have been demonstrated for CO_2/N_2 using a graphene/ionic liquid hybrid [134] and a selectivity ratio of 97 is reported by Jin *et al* [135] with iron intercalated reduced GO membranes. With mounting environmental and societal problems that could be answered by 2D membranes, improvements and physical insights demonstrated in the coming decade will be pivotal for their industrial and commercial viability.

Acknowledgment

The authors thank I Silkina, L Dolby and A Thorneywork for proof reading, advice and essential support. M C acknowledges funding from an EPSRC Doctoral Training Award (EP/L016087/1). U F K acknowledges funding from the ERC Consolidator Grant DesignerPores No. 647144.

ORCID iDs

M Caglar https://orcid.org/0000-0001-7547-1817
U F Keyser https://orcid.org/0000-0003-3188-5414

References

[1] Varcoe J R *et al* 2014 *Energy Environ. Sci.* **7** 3135–91
[2] Yin J, Zhang Z, Li X, Zhou J and Guo W 2012 *Nano Lett.* **12** 1736–41
[3] Siria A, Bocquet M L and Bocquet L 2017 *Nat. Rev. Chem.* **1** 0091
[4] Aliprandi A, Pakulski D, Ciesielski A and Samorì P 2017 *ACS Nano* **11** 10654–8
[5] Ghaffour N, Missimer T M and Amy G L 2013 *Desalination* **309** 197–207
[6] Luo T, Abdu S and Wessling M 2018 *J. Membr. Sci.* **555** 429–54
[7] Kim D K, Duan C, Chen Y F and Majumdar A 2010 *Microfluid. Nanofluid.* **9** 1215–24
[8] Caglar M *et al* 2020 *ACS Nano* **14** 2729–38
[9] Kasianowicz J J, Brandin E, Branton D and Deamer D W 1996 *Proc. Natl. Acad. Sci. USA* **93** 13770–3
[10] Gu Z, Zhang Y, Luan B and Zhou R 2016 *Soft Matter* **12** 817–23
[11] Sahu S and Zwolak M 2019 *Rev. Mod. Phys.* **91** 21004
[12] Walker M I, Ubych K, Saraswat V, Chalklen E A, Braeuninger-Weimer P, Caneva S, Weatherup R S, Hofmann S and Keyser U F 2017 *ACS Nano* **11** 1340–6
[13] Cohen-Tanugi D and Grossman J C 2012 *Nano Lett.* **12** 3602–8
[14] Kang Y, Zhang Z, Shi H, Zhang J, Liang L, Wang Q, Ågren H and Tu Y 2014 *Nanoscale* **6** 10666–72
[15] Bunch J S, Verbridge S S, Alden J S, Van Der Zande A M, Parpia J M, Craighead H G and McEuen P L 2008 *Nano Lett.* **8** 2458–62
[16] Mogg L, Zhang S, Hao G P, Gopinadhan K, Barry D, Liu B L, Cheng H M, Geim A K and Lozada-Hidalgo M 2019 *Nat. Commun.* **10** 4243
[17] Rollings R C, Kuan A T and Golovchenko J A 2016 *Nat. Commun.* **7** 11408

[18] O'Hern S C, Boutilier M S, Idrobo J C, Song Y, Kong J, Laoui T, Atieh M and Karnik R 2014 *Nano Lett.* **14** 1234–41
[19] Chin H T, Lee J J, Hofmann M and Hsieh Y P 2018 *Sci. Rep.* **8** 3–8
[20] Zurutuza A and Marinelli C 2014 *Nat. Nanotechnol.* **9** 730–4
[21] Lin L, Peng H and Liu Z 2019 *Nat. Mater.* **18** 520–4
[22] Kobayashi T *et al* 2013 *Appl. Phys. Lett.* **102** 1–5
[23] Guirguis A, Maina J W, Kong L, Henderson L C, Rana A, Li L H, Majumder M and Dumée L F 2020 *Carbon* **155** 660–73
[24] Graf M, Lihter M, Unuchek D, Sarathy A, Leburton J P, Kis A and Radenovic A 2019 *Joule* **3** 1549–64
[25] Koenig S P, Wang L, Pellegrino J and Bunch J S 2012 *Nat. Nanotechnol.* **7** 728–32
[26] Rabchinskii M K *et al* 2016 *J. Phys. Chem.* C **120** 28261–9
[27] Weber M, Koonkaew B, Balme S, Utke I, Picaud F, Iatsunskyi I, Coy E, Miele P and Bechelany M 2017 *ACS Appl. Mater. Interfaces* **9** 16669–78
[28] Grosjean B, Bocquet M L and Vuilleumier R 2019 *Nat. Commun.* **10** 1–8
[29] Goldman D E 1943 *J. Gen. Physiol.* **27** 37–60
[30] Hille B 1978 *Biophys. J.* **22** 283–94
[31] Alvarez O and Latorre R 2017 *J. Gen. Physiol.* **149** 911–20
[32] Guardiani C, Gibby W A, Barabash M L, Luchinsky D G and McClintock P V 2019 *RSC Adv.* **9** 20402–14
[33] Wen C, Zeng S, Li S, Zhang Z and Zhang S L 2019 *Anal. Chem.* **91** 14597–604
[34] Lee C, Joly L, Siria A, Biance A L, Fulcrand R and Bocquet L 2012 *Nano Lett.* **12** 4037–44
[35] Somasundaran P 2006 *Encyclopedia of Surface and Colloid Science* vol 2 (Boca Raton, FL: CRC Press)
[36] Fendler J H 1996 *Adv. Mater.* **8** 260
[37] Smith A M, Lee A A and Perkin S 2016 *J. Phys. Chem. Lett.* **7** 2157–63
[38] Poggioli A R, Siria A and Bocquet L 2019 *J. Phys. Chem.* B **123** 1171–85
[39] Kowalczyk S W, Grosberg A Y, Rabin Y and Dekker C 2011 *Nanotechnology* **22** 315101
[40] Cervera J, Ramirez P, Mafe S and Stroeve P 2011 *Electrochim. Acta* **56** 4504–11
[41] Hall J E 1975 *J. Gen. Physiol.* **66** 531–2
[42] Coulter W H 1953 *United States Pat. Off. Patentiert am* **20** 1953
[43] Bell N A, Chen K, Ghosal S, Ricci M and Keyser U F 2017 *Nat. Commun.* **8** 1–8
[44] Wanunu M, Sutin J, McNally B, Chow A and Meller A 2008 *Biophys. J.* **95** 4716–25
[45] Varongchayakul N, Song J, Meller A and Grinstaff M W 2018 *Chem. Soc. Rev.* **47** 8512–24
[46] De Fazio D *et al* 2019 *ACS Nano* **13** 8926–35
[47] Wi S, Kim H, Chen M, Nam H, Guo L J, Meyhofer E and Liang X 2014 *ACS Nano* **8** 5270–81
[48] Wang H, Liu F, Fu W, Fang Z, Zhou W and Liu Z 2014 *Nanoscale* **6** 12250–72
[49] Radisavljevic B, Radenovic A, Brivio J, Giacometti V and Kis A 2011 *Nat. Nanotechnol.* **6** 147–50
[50] Kwok H, Briggs K and Tabard-Cossa V 2014 *PLoS One* **9** e92880
[51] Kuan A T, Lu B, Xie P, Szalay T and Golovchenko J A 2015 *Appl. Phys. Lett.* **106** 203109
[52] Feng J *et al* 2015 *Nano Lett.* **15** 3431–8
[53] Zrehen A, Gilboa T and Meller A 2017 *Nanoscale* **9** 16437–45
[54] Danda G, Masih Das P and Drndić M 2018 *2D Mater.* **5** 035011
[55] Lima L M, Fu W, Jiang L, Kros A and Schneider G F 2016 *Nanoscale* **8** 18646–53
[56] Van Der Heyden F H, Stein D, Besteman K, Lemay S G and Dekker C 2006 *Phys. Rev. Lett.* **96** 1–4
[57] Besteman K, Zevenbergen M A and Lemay S G 2005 *Phys. Rev.* E **72** 1–9
[58] Besteman K, Zevenbergen M A, Heering H A and Lemay S G 2004 *Phys. Rev. Lett.* **93** 4–7
[59] Tabaei S R, Ng W B, Cho S J and Cho N J 2016 *ACS Appl. Mater. Interfaces* **8** 11875–80
[60] Ang P K *et al* 2010 *ACS Nano* **4** 7387–94
[61] Kim M, Nabeya S, Nandi D K, Suzuki K, Kim H M, Cho S Y, Kim K B and Kim S H 2019 *ACS Omega* **4** 11126–34
[62] Gilbert S M, Dunn G, Azizi A, Pham T, Shevitski B, Dimitrov E, Liu S, Aloni S and Zettl A 2017 *Sci. Rep.* **7** 1–7
[63] Thiruraman J P *et al* 2018 *Nano Lett.* **18** 1651–9
[64] Liu K, Feng J, Kis A and Radenovic A 2014 *ACS Nano* **8** 2504–11
[65] Deng Y, Huang Q, Zhao Y, Zhou D, Ying C and Wang D 2017 *Nanotechnology* **28** 045302
[66] Martin M B *et al* 2014 *ACS Nano* **8** 7890–5
[67] Surwade S P, Smirnov S N, Vlassiouk I V, Unocic R R, Veith G M, Dai S and Mahurin S M 2015 *Nat. Nanotechnol.* **10** 459–64
[68] Alem N, Erni R, Kisielowski C, Rossell M D, Gannett W and Zettl A 2009 *Phys. Rev.* B **80** 1–7
[69] Meyer J C, Chuvilin A, Algara-Siller G, Biskupek J and Kaiser U 2009 *Nano Lett.* **9** 2683–9
[70] Russo C J and Golovchenko J A 2012 *Proc. Natl. Acad. Sci. USA* **109** 5953–7
[71] Lehtinen O, Kotakoski J, Krasheninnikov A V, Tolvanen A, Nordlund K and Keinonen J 2010 *Phys. Rev.* B **81** 1–4
[72] Yoon K *et al* 2016 *ACS Nano* **10** 8376–84
[73] Graf M *et al* 2019 *Nat. Protocols* **14** 1130–68
[74] Parkin W M *et al* 2016 *ACS Nano* **10** 4134–42
[75] Xu K *et al* 2019 *Phys. Rev.* B **99** 1–13
[76] Krasheninnikov A V and Banhart F 2007 *Nat. Mater.* **6** 723–33
[77] Egerton R F 2013 *Microsc. Microanal.* **19** 479–86
[78] Schneider G F, Kowalczyk S W, Calado V E, Pandraud G, Zandbergen H W, Vandersypen L M and Dekker C 2010 *Nano Lett.* **10** 3163–7
[79] Zobelli A, Gloter A, Ewels C P, Seifert G and Colliex C 2007 *Phys. Rev.* B **75** 1–9
[80] Smith B W and Luzzi D E 2001 *J. Appl. Phys.* **90** 3509–15
[81] Crespi V H, Chopra N G, Cohen M L, Zettl A and Louie S G 1996 *Phys. Rev.* B **54** 5927–31
[82] Girit Ç Ö *et al* 2009 *Science* **323** 1705–8
[83] Li J, Stein D, McMullan C, Branton D, Aziz M J and Golovchenko J A 2001 *Nature* **412** 166–9
[84] Fischbein M D and Drndić M 2008 *Appl. Phys. Lett.* **93** 2006–9
[85] Gopinadhan K *et al* 2019 *Science* **363** 145–8
[86] Nie L, Goh K, Wang Y, Lee J, Huang Y, Enis Karahan H E, Zhou K, Guiver M D and Bae T H 2020 *Sci. Adv.* **6** eaaz9184
[87] Loan P T K, Zhang W, Lin C T, Wei K H, Li L J and Chen C H 2014 *Adv. Mater.* **26** 4838–44
[88] Zhang X, Wen Q, Wang L, Ding L, Yang J, Ji D, Zhang Y, Jiang L and Guo W 2019 *ACS Nano* **13** 4238–45
[89] Zhao Y, Huang D, Su J and Gao S 2020 *J. Phys. Chem.* C **124** 17320–30
[90] Mouterde T, Keerthi A, Poggioli A R, Dar S A, Siria A, Geim A K, Bocquet L and Radha B 2019 *Nature* **567** 87–90
[91] Esfandiar A, Radha B, Wang F C, Yang Q, Hu S, Garaj S, Nair R R, Geim A K and Gopinadhan K 2017 *Science* **358** 511–13

[92] Chen X *et al* 2020 *Adv. Mater.* **32** 1–7
[93] Ding L, Xiao D, Lu Z, Deng J, Wei Y, Caro J and Wang H 2020 *Angew. Chem. Int. Ed.* **59** 8720–6
[94] Lin Y C *et al* 2014 *Nano Lett.* **14** 6936–41
[95] Thomas M, Corry B and Hilder T A 2014 *Small* **10** 1453–65
[96] Zhao S, Xue J and Kang W 2013 *J. Chem. Phys.* **139** 114702
[97] He Z, Zhou J, Lu X and Corry B 2013 *ACS Nano* **7** 10148–57
[98] Cohen-Tanugi D and Grossman J C 2015 *Desalination* **366** 59–70
[99] Hirunpinyopas W, Prestat E, Iamprasertkun P, Bissett M A and Dryfe R A 2020 *2D Mater.* **7** 015030
[100] Hong S, Constans C, Surmani Martins M V, Seow Y C, Guevara Carrió J A and Garaj S 2017 *Nano Lett.* **17** 728–32
[101] Feng J *et al* 2016 *Nature* **536** 197–200
[102] Ghosh M, Jorissen K F, Wood J A and Lammertink R G 2018 *J. Phys. Chem. Lett.* **9** 6339–44
[103] Wyss R M, Tian T, Yazda K, Park H G and Shih C J 2019 *Nano Lett.* **19** 6400–9
[104] Siria A, Poncharal P, Biance A L, Fulcrand R, Blase X, Purcell S T and Bocquet L 2013 *Nature* **494** 455–8
[105] Thiruraman J P, Masih Das P and Drndić M 2020 *ACS Nano* **14** 11831–45
[106] Hirunpinyopas W, Prestat E, Worrall S D, Haigh S J, Dryfe R A and Bissett M A 2017 *ACS Nano* **11** 11082–90
[107] Macha M, Marion S, Nandigana V V and Radenovic A 2019 *Nat. Rev. Mater.* **4** 588–605
[108] Klaysom C, Cath T Y, Depuydt T and Vankelecom I F 2013 *Chem. Soc. Rev.* **42** 6959–89
[109] Pakulski D, Czepa W, Buffa S D, Ciesielski A and Samorì P 2020 *Adv. Funct. Mater.* **30** 1–21
[110] Athreya N, Milenkovic O and Leburton J P 2020 *npj 2D Mater. Appl.* **4** 1–8
[111] Danda G *et al* 2017 *ACS Nano* **11** 1937–45
[112] Merchant C A *et al* 2010 *Nano Lett.* **10** 2915–21
[113] Zhou Z, Hu Y, Wang H, Xu Z, Wang W, Bai X, Shan X and Lu X 2013 *Sci. Rep.* **3** 1–5
[114] Garaj S, Hubbard W, Reina A, Kong J, Branton D and Golovchenko J A 2010 *Nature* **467** 190–3
[115] Garaj S, Liu S, Golovchenko J A and Branton D 2013 *Proc. Natl Acad. Sci. USA* **110** 12192–6
[116] Thakur M, Macha M, Chernev A, Graf M, Lihter M, Deen J, Tripathi M, Kis A and Radenovic A 2020 *Small Methods* **4** 2000072
[117] Graf M, Lihter M, Altus D, Marion S and Radenovic A 2019 *Nano Lett.* **19** 9075–83
[118] Si W, Zhang Y, Sha J and Chen Y 2018 *Nanoscale* **10** 19450–8
[119] Jiang C, Li Q, Huang J, Bi S, Ji R and Guo Q 2020 *ACS Appl. Mater. Interfaces* **12** 41991–8
[120] Noyce S G, Doherty J L, Zauscher S and Franklin A D 2020 *ACS Nano* **14** 11637–47
[121] Heerema S J, Schneider G F, Rozemuller M, Vicarelli L, Zandbergen H W and Dekker C 2015 *Nanotechnology* **26** 074001
[122] Liu G, Rumyantsev S, Shur M S and Balandin A A 2013 *Appl. Phys. Lett.* **102** 093111
[123] Zhang Y, Zhou Y, Li Z, Chen H, Zhang L and Fan J 2020 *Nanoscale* **12** 10026–34
[124] Rodríguez B A, Pérez-Caro M, Alencar R S, Souza Filho A G and Albino Aguiar J 2020 *J. Appl. Phys.* **127** 044901
[125] Ganguli A, Faramarzi V, Mostafa A, Hwang M T, You S and Bashir R 2020 *Adv. Funct. Mater.* **30** 1–9
[126] Kidambi P R, Mariappan D D, Dee N T, Vyatskikh A, Zhang S, Karnik R and Hart A J 2018 *ACS Appl. Mater. Interfaces* **10** 10369–78
[127] Xin H and Li W 2018 *Appl. Phys. Rev.* **5** 031105
[128] Gadaleta A, Sempere C, Gravelle S, Siria A, Fulcrand R, Ybert C and Bocquet L 2014 *Phys. Fluids* **26** 012005
[129] Su J, Ji D, Tang J, Li H, Feng Y, Cao L, Jiang L and Guo W 2018 *Chin. J. Chem.* **36** 417–20
[130] Lan W J, Holden D A and White H S 2011 *J. Am. Chem. Soc.* **133** 13300–3
[131] Joshi N, Hayasaka T, Liu Y, Liu H, Oliveira O N and Lin L 2018 *Microchim. Acta* **185** 213
[132] Kim S, Wang H and Lee Y M 2019 *Angew. Chem. Int. Ed.* **58** 17512–27
[133] Gao S, Wang D, Fang W and Jin J 2020 *Adv. Mater. Technol.* **5** 1901069
[134] Guo W, Mahurin S M, Unocic R R, Luo H and Dai S 2020 *Nano Lett.* 7995–8000
[135] Jin X *et al* 2020 *Adv. Mater.* **32** 1–10